

# Tuning the Oxygen Balance of Energetic Composites: Crystallization of ADN/Secondary Explosives Mixtures by Spray Flash Evaporation

Emeline Lobry,<sup>\*[a]</sup> Jean-Edouard Berthe,<sup>[a]</sup> Jakob Hübner,<sup>[a]</sup> Fabien Schnell,<sup>[a]</sup> and Denis Spitzer<sup>[a]</sup>

**Abstract:** New energetic composites with enhanced reactive performances while allowing the safe handling according to their sensitivity thresholds are presented. This paper combines different approaches: the intimate contact between the compounds, the particle size reduction and the processing of composite materials to maintain the oxygen balance close to zero. The Spray Flash Evaporation process enables the fast crystallization at the submicron scale by combining an oxidizer, ammonium dinitramide

ADN and two secondary explosives (RDX and HMX). The morphologies of the particles were analyzed and compared with slow evaporation tests. An intimate mixing between the two components (crystallized by SFE) is highlighted and core-shell structure is evidenced by advanced techniques such as 2D and 3D confocal Raman microscopy. The composites offer outstanding energetic performances compared to sole explosives. It paves the way to new energetic compositions based on current materials.

**Keywords:** Crystallization · Composites · Spray flash evaporation · Energetic materials · Confocal Raman spectroscopy

## 1 Introduction

Processing of explosives at the sub-micro or nanoscale has gathered more importance within the last years to overcome safety troubles and to improve energetic performance [1]. In this context, size reduction implies the recrystallization of micrometric crystals onto the submicron- or nanoscale. The size reduction includes desensitization to impact, heat, friction or electrostatic discharge depending on the formulated compounds [2–5].

Several top down or bottom up size reduction processes have been developed with their own specific advantages and disadvantages [6]. Few examples regarding energetic materials are based on top down processes. Some authors report the use of milling [7,8] though the risk of unintentional decomposition initiation due to high energy transfer to the energetic compounds remains high. Contrary, bottom-up spray processes like electrospray [9], rapid expansion of supercritical solutions (RESS) [10,11] or spray flash evaporation (SFE) yield better control of heat transfer and reduce thus the risk of unintentional decomposition.

A further strategy to enhance energetic performances and sensitivity thresholds of secondary explosives is the formulation of composite materials. Desensitization of energetic compounds is enabled for instance by combining secondary explosives with polymers [12–14], with further secondary explosives [15,16], with metal oxides [17] or with graphite or nanodiamonds [18,19]. The formulation of such composites improves the mechanical stability, and decreases sensitivity against friction, impact and ESD [18]. Furthermore, additives enable the control of particles size and

morphology. Thus, Sèvre *et al.* [15] demonstrated that hexanitrostilbene (HNS) acts as growth inhibitor during TNT crystallization. In the same way poly(vinylpyrrolidone) PVP added to RDX for recrystallization helps to better control reactivity. It also acts on nucleation providing reduced particle sizes compared to recrystallization performed in same operating conditions but without additive [20].

Anyway, the main challenge by increasing the explosive performances is to maintain safety properties like sensitivity thresholds. The oxygen balance of pyrotechnic composition seems to play a significant role on both the reactive performances and safety properties of explosives. The oxygen balance OB is defined as

$$OB = \frac{1600(d - 2a - \frac{b}{2})}{M}, \quad (1)$$

where  $a$ ,  $b$ ,  $c$ ,  $d$  represent the number of specific atoms for a molecule  $C_aH_bN_cO_d$  and  $M$  is the molecular mass. A zero-oxygen balance corresponds to a molecule which contains just enough oxygen to form carbon dioxide from carbon, water from hydrogen atoms, sulfur dioxide from sulfur,

[a] E. Lobry, J.-E. Berthe, J. Hübner, F. Schnell, D. Spitzer  
*Nanomatériaux pour les Systèmes Sous Sollicitations Extrêmes (NS3E) (UMR 3208 ISL/CNRS/Université de Strasbourg), Institut franco-allemand de recherches de Saint-Louis (ISL) 5, rue du Général Cassagnou BP 70034 68301 SAINT-LOUIS Cedex FRANCE*  
\*e-mail: elobry@unistra.fr

 Supporting information for this article is available on the WWW under <https://doi.org/10.1002/prep.202000090>

metal oxide from metals, with no excess. So, it limits the products of decomposition. Chemicals with a positive OB contains more oxygen than needed and are defined as oxidizers in pyrotechnical terms. Contrary, chemicals with a negative OB contain less oxygen than is needed. The combustion will then be incomplete, and large amount of toxic gases like carbon monoxide will be present.

However, compounds with an OB close to zero demonstrate improved brisance [21] i.e. the shattering capability of explosives, higher heats of explosion [22] and increased energy release [23]. OB correlates very poorly with sensitivity and is not a reasonable criterion by itself. Yet some publications reports that impact sensitivity thresholds may decrease by changing OB. The impact sensitivity is halved for OB ranging from  $-3$  to  $+3\%$  for polynitro-explosive compounds [24]. One example is Amatol. Amatol is a mixture of ammonium nitrate and TNT with an OB of 1%. It releases a 30% higher heat of explosion than pure TNT. Thus, research is focused on the synthesis of new explosives with an OB of zero such as octanitrocubane (ONC) [25] or tetrazino-tetrazine-tetraoxide (TTTO) [26]. Although they may provide better energetic performances than the powerful secondary explosive 2,4,6,8,10,12,-hexanitro-2,4,6,8,10,12-hexaazaisowurtzitane CL-20 as computed by a density functional theory simulation, their productions are expensive since sophisticated synthesis routines with low yield are required. Most of the studies concern theoretical approaches that demonstrate outstanding performances in term of reactivity or sensitivity but limited experimental results [27,28].

In the prospect of improving energetic materials efficiency and handling, presented formulations with oxygen balance close to zero appear a promising way. The syntheses of new submicron composites are aimed to combine the advantages of the different strategies i.e. particles downscaling and mixing of compounds. The oxygen balance is tuned by combining an oxidizer and a secondary explosive. The secondary explosives 1,3,5-trinitroperhydro-1,3,5-triazine (RDX) and 1,3,5,7-tetranitro-1,3,5,7-tetrazocane (HMX) were chosen according to their broad use in the military field. RDX is one of the most frequently used secondary explosives. Due to its good energetic performances and its reasonable costs, it is used in military and civilian applications. Thus, it is a part of the most important explosive compositions e.g. semtex, C4 or composition B [29]. Another common explosive utilized in the military field is HMX. HMX is inter alia characterized by a higher detonation velocity than RDX (Table 1). It is more and more used in explosive compositions and munitions for military

applications and may overtake RDX. Explosives are characterized inter alia by their detonation velocity  $V_D$ , their deflagration-to-detonation transition distance (DDTD), their brisance and their oxygen balance (OB). Some of these characteristics available in literature are summed-up in Table 1.

ADN is used as oxidizer within later presented energetic formulations. ADN draws attention in energetic material science because it is intended to replace other oxidizers such as ammonium perchlorate in high performance solid rocket boosters as an environmentally friendly smokeless propellant [31]. Furthermore, it offers higher specific impulse compared to ammonium perchlorate. Moreover, it presents some benefits to public health and environment since it is unchlorinated. However, ADN is also defined by its high hygroscopicity [32,33]. The size reduction is performed by recrystallization on the submicron scale using the Spray Flash Evaporation process. This technology proved its ability to produce submicron explosives and oxidants [34,35] as well as non-energetic organic compounds, co-crystals and diverse composites [36,37]. It is based on the spray of a superheated solution. The droplets are generated in the flash reactor and the large pressure drop leads to a sudden solvent evaporation and subsequent crystallization [38]. The aim is to obtain submicron composite particles from an intimate mix of both components. Within this work, the obtained materials are characterized in terms of size, morphology, molecular arrangement and thermal decomposition. Further submicron scaled ADN/secondary explosive composites are compared with micron sized mixtures produced by slow evaporation. Finally, sensitivity thresholds and reactivity of ADN/secondary explosive composites are compared with pristine materials (ADN and secondary explosives).

## 2 Experimental Section

### 2.1 Chemicals

ADN, RDX and HMX were purchased from EURENCO. All compounds were dried in an oven at  $70^\circ\text{C}$  for 4 h before further use. Their main properties are summarized in Table 2. Ethyl acetate (99.5%), methyl acetate (99%) and acetone (HPLC quality) were purchased from Carl Roth GmbH.

The solubilities of each component in the diverse solvents are given under standard conditions except mentioned.

**Table 1.** Characteristics of common explosives [29,30].

Explosives	$\rho$ , g $\text{cm}^{-3}$	OB, %	$V_D$ (theory), $\text{km s}^{-1}$
RDX ( $\alpha$ )	1.82	-21.6	8.7 @1.76
HMX ( $\beta$ )	1.91	-21.6	9.1 @1.9

**Table 2.** Properties of the explosives and ADN.

Materials	$\alpha$ -RDX	$\beta$ -HMX	ADN
OB, %	-21.6	-21.6	25.8
MP, °C	204	278	95
DT, °C	237	287	127
$V_D$ , $m\ s^{-1}$	8700 [29] (density $1.72\ g\ cm^{-3}$ )	9100 [29] (density $1.9\ g\ cm^{-3}$ )	6300 [39]
Solubility at 25 °C	- Acetone: 8.2 wt.% [40] - Ethyl acetate or methyl acetate: < 0.1 wt.%	- Acetone: 2.8 wt.% [40] - Ethyl acetate: 0.34 wt.% - Methyl acetate: 0.49 wt.%	- Ethyl acetate: 1.23 wt.% [35] - Methyl acetate: 7.13 wt.% [35] - Acetone: 47.6 wt.% at 32 °C [41]
$D_{50}$ , $\mu m$ neat product	3.69 $\mu m$ spherical, ovoidal and polyhedral shapes	0.7 $\mu m$ , large distribution	Acicular, 200 $\mu m$

## 2.2 Preparation Methods

### 2.2.1 Precursor Solutions

#### 2.2.1.1 Pure compounds

For the pure component experiments, solutions of 500 mL with respectively 1 wt.% of RDX were dissolved in acetone. For HMX, 1 wt.% and 0.3 wt.% of product was dissolved 500 mL of acetone respectively methyl acetate.

#### 2.2.1.2 Composite Mixtures

For the composites, the solutions were prepared in order to adjust the oxygen balance *OB* defined by equation (1) at -1 %. The ratio between the oxidizer and the explosives were adjusted in the following proportion ADN/RDX 1/1.25, ADN/HMX 1/1.25 in weight diluted at 2 wt.% for ADN/RDX, and 0.6 wt.% for ADN/HMX in the appropriate solvent.

#### 2.2.2 Crystallization by Spray Flash Evaporation (SFE)

The Spray Flash Evaporation process consists in spraying a superheated solution through a heated 80  $\mu m$  diameter hollow cone nozzle (Brumstyl, France) in a permanent evacuated atomization chamber. The pressure inside the atomization chamber amounts 500 Pa during the spray process.

The high pressure drop and inlet temperature induce fast evaporation of the generated droplets and thus quick crystallization at the sub-micro scale. A filter with a mesh of 50  $\mu m$  was used to recover the product.

Table 3 gives the process parameters for pure explosives and composite materials of ADN/secondary explosive crystallized by SFE.

Due to the low degradation temperature of ADN, as presented in Table 2, the recrystallizations by SFE were performed at a temperature set to 110 °C.

#### 2.2.3 Crystallization by Slow Evaporation

Slow evaporation crystallizations were performed by evaporating described solutions at a constant temperature of 22 °C under ambient pressure for 48 h. The composite materials were recovered in a vessel for further analyses. These compositions are mentioned with a star (\*) in Table 3.

## 2.3 Characterization

### 2.3.1 Morphology and Chemical Analysis

Morphologies of the composites were imaged by a FEI Nova (USA) NanoSEM 450 Scanning electronic microscopy (SEM) equipped with a field emission gun operating at

**Table 3.** Operating conditions for the crystallization by SFE and slow evaporation (\*) at 0.1 MPa, 22 °C.

Compound or Mixture	T <sub>N</sub> , °C	Solvent	P <sub>N</sub> , MPa	Name
RDX	110	Acetone	4	RDX-S1P1
			2	RDX-S1P2
ADN/RDX 2 wt.%. 1/1.25		Acetone*	4	ADN/RDX-S1P1
HMX		Acetone	2	ADN/RDX-S1P2
			4	HMX-S1P1
			2	HMX-S1P2
ADN/HMX 0.6 wt.%. (1/1.25)		Methyl acetate		HMX-S2P2
		Acetone	4	ADN/HMX-S1P1
			2	ADN/HMX-S1P2
		Methyl acetate*	2	ADN/HMX-S2P2

10 kW (SE detector). Samples were covered by an 8 nm gold layer. The chamber pressure was <1 mPa during the measurements.

X-Ray powder diffraction (XRPD) was performed on a Bruker (Karlsruhe, Germany) D8 apparatus with LinxEye detector (copper anode  $h\gamma=8.05$  keV,  $\lambda_{Cu}=1.54$  Å) in Bragg-Brentano geometry. Crystallite size ( $D$ ) was determined with Scherrer's equation, following:

$$D = \frac{K^* \lambda_{Cu}}{\beta^* \cos \theta} \quad (2)$$

Where  $K$  is a constant linked to apparatus given at 0.89,  $\beta$  is the full width at half-maximum peak, and  $\theta$  the corresponding angle.

Raman spectroscopy was performed on a Renishaw (Wotton-under-edge, UK) InVia device. Linear polarized laser light with a wavelength of 633 nm was used for sample excitation.

2-dimensional and 3-dimensional confocal Raman maps were recorded on a LabRam HR Evolution microscope (HORIBA, France). Single point spectra were obtained by sample excitation with linear polarized illumination light from a 532 nm diode laser with an adjusted output power of 13.5 mW at an acquisition time of 2 s per spectrum. The laser light was focused onto the sample through a 100x 0.9NA objective. Raman scattered photons were collected by the same objectives in back reflection. Scattered light passed an edge filter, a confocal aperture with a diameter adjusted to 200 nm and a diffraction grating with 300 lines/mm before hitting a deep cooled CCD camera (-60 °C). Confocal Raman maps were calculated and depicted using Lab-Spec Spectroscopy Suite 6.4.4. (HORIBA; Paris, France).

X-ray photoelectron spectroscopy (XPS) analysis with XPS VG SCIENTA SES-2002 spectrometer (Denver, USA). Monochromatic X-Ray Al K $\alpha$  ( $h\gamma=1.49$  keV,  $\lambda_{Al}=8.34$  Å) source was used and data were processed by CasaXPS software.

Differential scanning calorimetry (DSC) and thermogravimetric analysis (TGA) were performed with Q600 from TA Instruments under nitrogen flow. Sample of few mg is put in a gold sealed crucible.

### 2.3.2 Sensitivity and Reactivity

The thresholds mentioned are the value for which 6 tested samples provided no reaction. Impact sensitivities were evaluated with a standard BAM Fall Hammer. Sensitivity to friction was measured on a Julius Peter device (BAM friction test). Samples are placed on a rough ceramic substrate and a ceramic stick exerts a force (relative position of weight suspending by a lever) corresponding to a friction energy. Sensitivity to electrostatic discharge was tested by using ESD 2008 (OZM Research, Czech Republic). Samples are brought between two electrodes. The energy can be adjusted by tuning capacitance and voltage.

Studies of sample decomposition modes were performed with PMMA (poly(methyl methacrylate)) tubes filled with the pyrotechnic composition. The tubes have a length of 150 mm with an inner diameter of 3 mm and outer diameter of 25 mm. The first 5 mm of the tubes were loaded with an Al/CuO nanothermite to ignite the diverse composites. Loads were prepared by measuring powder density at regular intervals. Airbag igniter (Autoliv NCS) was filled with two nanothermites to ignite the device. The decomposition reaction was recorded with fast camera (Photron FASTCAM SA-Z) until 2.10<sup>5</sup> fps. The tests were repeated three times and averaged in order to compute detonation velocity  $V_D$  and deflagration-to-detonation transition distance DDTD. Distance between decomposition front and loading material extremity (ignition side) was measured on video pictures at regular intervals.

## 3 Results and Discussion

### 3.1 Recrystallization of Secondary Explosive by Spray Flash Evaporation

The obtained results are summarized in Table 4.

Crystallization of ADN was successfully performed by Berthe *et al.* for a nozzle pressure of 2 MPa and a nozzle temperature of 110 °C in ethyl or methyl acetate [35]. Spherical particles of ADN were produced with mean size of 37 nm +/- 5 nm.

**Table 4.** Morphology and polymorphism for the crystallization of the secondary explosives by SFE at  $T_N=110$  °C (\*L: length, W: width), <sup>[a]</sup>see Figure 3, <sup>[b]</sup>see Figure 7.

Sample	Solvent	P <sub>N</sub> , MPa	Morphology	Size, μm	Span	Polymorphism
RDX-S1P1	Acetone	4	spherical	0.50	2.14	$\alpha^a$
RDX-S1P2		2	spherical	0.32	2.82	
HMX-S1P1	Acetone	4	rod	L*: 2.65 W*: 1.07	L*: 2.37 W*: 1.86	$\gamma+\alpha^b$ (aged in $\alpha$ )
HMX-S1P2		2	spherical	0.15	4.7	$\gamma^b$ (aged in $\gamma+\alpha$ )
HMX-S2P2	Methyl acetate*	2	spherical	0.17	4.5	$\gamma+\beta^b$ (aged in $\gamma+\beta+\alpha$ )

In the same way, secondary explosive submicronic particles were obtained under the operating conditions described in Table 4. In the supplementary materials section, the SEM pictures and XRPD patterns are provided in Figure S1 and S2. Figure 1 depicts the particle size distributions. Anyway, recrystallization of RDX results always in spherical submicronic particles in  $\alpha$  form independently of the experimental conditions. Contrary, HMX appear in different morphologies and polymorphs according to the used solvents. The results are discussed in part 3.6.

### 3.2 Characterization of ADN/RDX Composites

The ADN/RDX S1P1 and S1P2 recrystallizations differ by the pressure applied on the precursor solutions (Table 3). The nozzle pressure drives directly the flowrate at the nozzle exit. Particles obtained by SFE exhibit a rod shaped and micrometric morphology in SEM images. They differ strongly

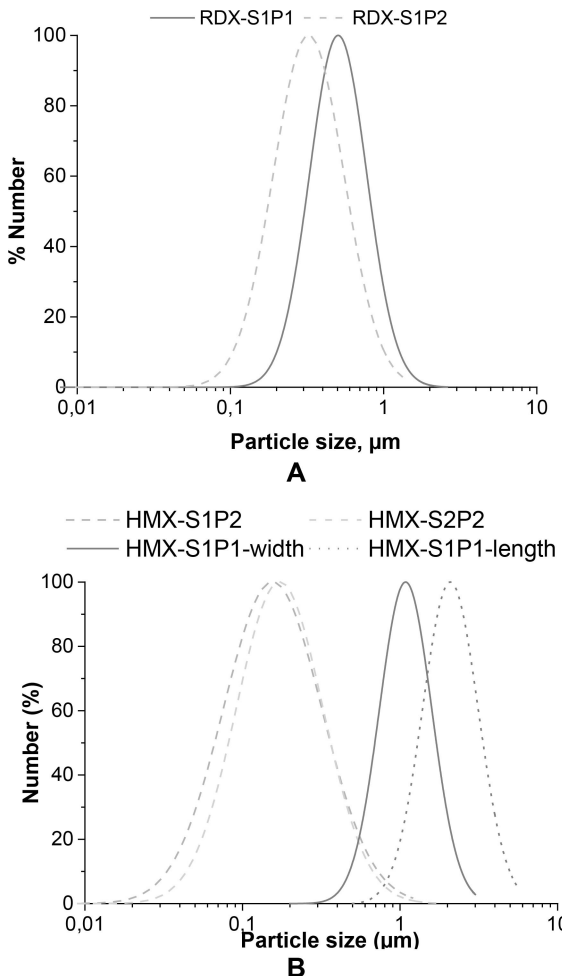


**Figure 1.** Particle size distribution of the secondary explosives crystallized by SFE (operating conditions see Table 4) for A- RDX and B- HMX.

from pure RDX particles appearing quite spherical in SEM images (see Figure S1 and Table 4).

SEM images of particles obtained by slow evaporation present particles produced with sizes of several hundreds of  $\mu\text{m}$  (Figure 2 and Figure 6A) contrary to sole explosives particles.

Figure 3 compares the XRPD diffraction patterns of pristine compounds, ADN/RDX-S1P1, ADN/RDX-S1P2 and ADN/RDX obtained by slow evaporation.

XRPD patterns of all ADN/RDX composites include all characteristic reflexes of ADN and RDX after recrystallization. Thus, the most stable orthorhombic  $\alpha$ -RDX is obtained for all conditions in the composites. However, RDX peaks appear less intense as shown in ADN/RDX-S1P2 Ram-

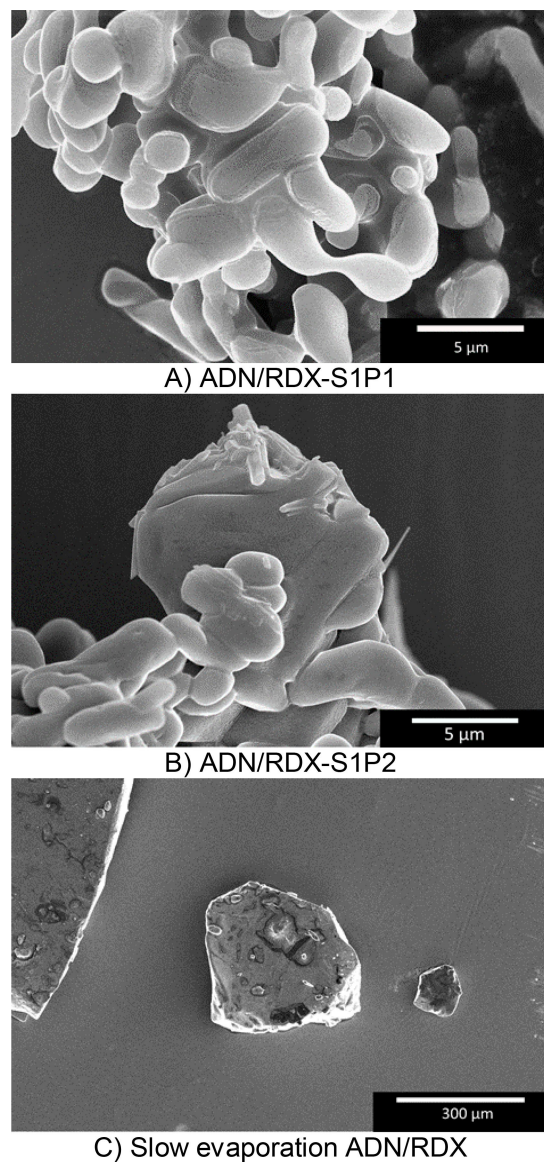


**Figure 2.** SEM images of A) ADN/RDX-S1P1 B) ADN/RDX-S1P2 C) Slow crystallization.

## Crystallization of ADN/Secondary Explosives Mixtures by Spray Flash Evaporation

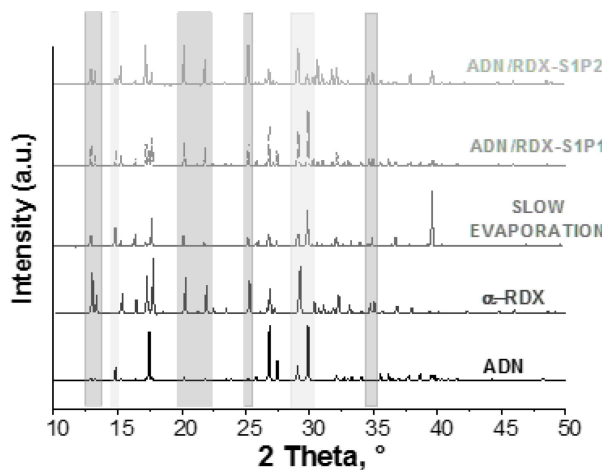


**Figure 3.** XRPD diffraction patterns of pristine ADN and RDX, ADN/RDX-S1P1, ADN/RDX-S1P2 and ADN/RDX obtained by slow evaporation.

an spectra (Figure S3). The sizes of the crystallites are given in Table 5 and obtained by using Scherrer equation (2).

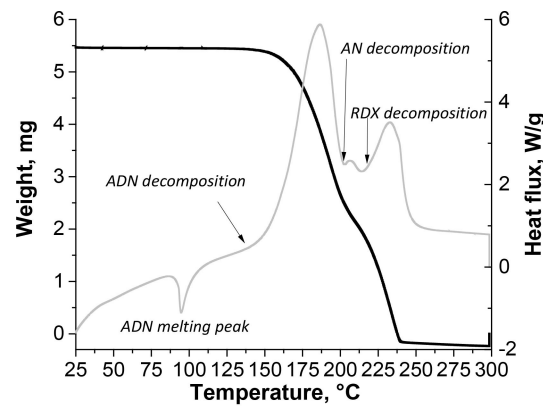
TGA-DSC analyses were performed on the different composites. The ADN melting peak is noted at 93.8 °C and the decomposition occurs around 125 °C for all ADN/RDX composites (Figure 4). Ammonium nitrate (AN) is formed due to the ADN decomposition [39,42,43]. The decomposition peak of RDX is obtained at 228 °C for all ADN/RDX composites. The different steps in the ADN decomposition (liquid ADN decomposition with AN formation and decomposition) are more evidenced with the thermogram corresponding to the compounds obtained by SFE, as previously underlined by Berthe *et al.*. These decomposition steps are confirmed by the weight curves.

<sup>1</sup>H-NMR confirmed the presence of both ADN and RDX within all ADN/RDX composites and the preservation of their mass fractions (Figure S4). These results confirm the reliability of the spray flash evaporation process since no degradation of the precursor compounds occurs during the recrystallization process.

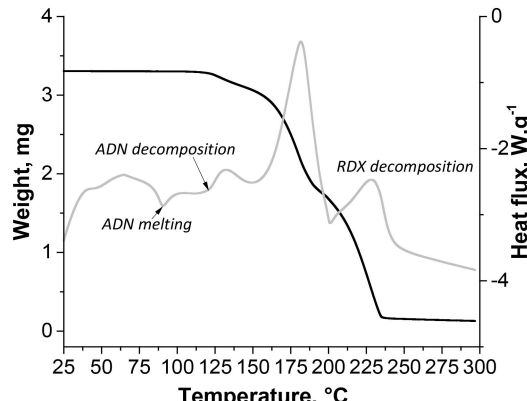
Although XRPD patterns enable the identification of both RDX and ADN in each mixture and that <sup>1</sup>H-NMR spectra confirm ratio conservation, it is impossible to distinguish both compounds on SEM images. Structure investigations

**Table 5.** Crystallographic forms and crystallite sizes for the ADN/RDX composites (calculation for  $2\theta = 14.98^\circ$ ).

Composite	Operating conditions	Crystallite size, nm	Polymorphism for the explosive
ADN/RDX	Slow evaporation	88.1	α
	RDX-S1P1	101.1	α
	RDX-S1P2	109.3	α



A)



B)

**Figure 4.** TGA-DSC thermograms for the ADN/RDX composite obtained either by slow evaporation (A) or by spray flash evaporation ADN/RDX-S1P2 (B).

of the organization of both materials within composite particles were performed by confocal Raman microscopy. For this approach, marker bands were chosen from Raman spectra of pristine ADN and secondary explosives. The Raman spectra of the pure compounds are shown Figure 5C. The marker bands of RDX and HMX appear at wavenumber regions where no signal can be detected within the Raman spectrum of pristine ADN [44,45]. RDX is evidenced by the vibration band ranging from  $3002 \text{ cm}^{-1}$  ( $-\text{CH}$  stretching) and ADN by the O—N—O bending identified at  $829 \text{ cm}^{-1}$ . (Figure S7). Raman maps depict the appearance of these marker bands in single Raman spectra as red respectively green pixels. If a single point spectrum contains both marker bands the associated pixel is colored in yellow. The shade of yellow ranges from orange over a bright yellow towards a light yellowish-green depending on the Raman intensities of the chosen marker bands. The confocal Raman microscopy images are depicted in Figure 5A. Red colored pixels depict the appearance of ADN marker bands and green colored pixels represent explosives marker bands, RDX in this section. Confocal Raman microscopy reveals

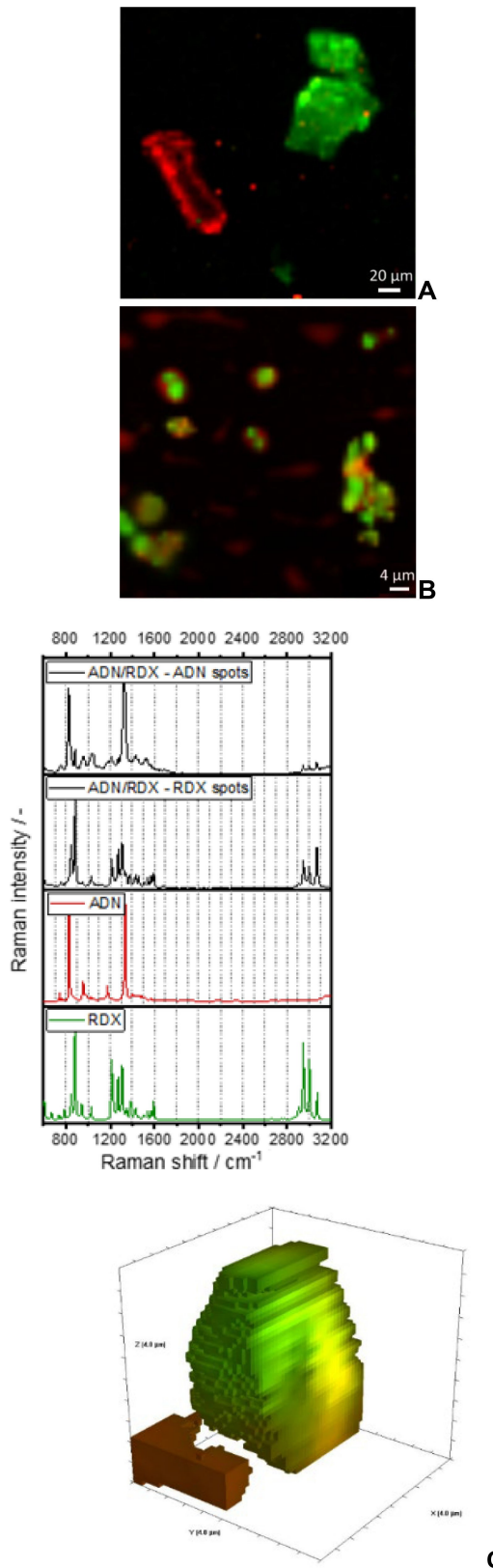


**Figure 5.** ADN/RDX composite obtained by A) slow evaporation and B) ADN/RDX S1P2 C) peak assignments and morphology.

that particles obtained by slow evaporation consist either of ADN or RDX. Consequently, slow evaporation process seems to be not suited for production of fine composite powders formed by ADN and secondary explosives. Contrary, RDX and ADN are found coupled in confocal Raman maps of SFE produced ADN/RDX composites. Figure 5C shows Raman spectra obtained at different locations of the particles. The spectra collection allows to obtain Figure 5C and to identify the particle morphology. Thus, RDX particles appear located on top of ADN droplets. It is assumed that SFE produced ADN/RDX composites are formed by RDX-ADN core-shell particles. The formation of the ADN droplet identified in Raman maps may occur by self-dissolution of hygroscopic ADN in ambient water during Raman measurements. XPS analysis were also performed on the particles. The details can be found in SI (Figure S5). With this technique, ADN decomposed due to ultra-high vacuum because of its low melting point and no evidence of ADN can be made on the particles surface after analysis. These disappointing results are however supporting the possibility of an ADN shell surrounding a core of RDX.

### 3.3 Characterization of ADN/HMX Composites

Three different composites were formulated varying in either the applied pressure (ADN/HMX-S1P1, ADN/HMX-S1P2) or the used solvent (ADN/HMX-S1P2, ADN/HMX-S2P2) (Table 3).

SEM images reveal (Figure 6) different particle morphologies depending on the applied pressure and on the solvent. ADN/HMX-S1P1 particles present a needle-shaped morphology with submicrometer widths and micrometer lengths. By decreasing the pressure, larger agglomerates are obtained. In contrast to ADN/HMX composites produced from acetone solutions, ADN/HMX-S2P2 is formed by submicron spheres and needle-shaped particles occurring much smaller than ADN/HMX-S1P1 and ADN/HMX-S1P2 particles.

XRPD diffraction patterns of pristine ADN, diverse HMX polymorphs and ADN/HMX composites are depicted in Figure 7. All ADN/HMX composites XRPD patterns provide the characteristic peaks of ADN and of diverse HMX polymorphs. Depending on the operating conditions, HMX appears in different polymorphic forms.

Process conditions trigger the formation of  $\alpha$ -HMX polymorph after aging whereas the raw product displays the  $\beta$ -form. The sizes of the crystallites are given in Table 6 and obtained by using Scherrer equation (2).

Thus, measured Raman spectra contain frequencies of both ADN and HMX as shown in Figure 8. Raman spectra of the diverse samples confirm the results obtained by XRPD. TGA-DSC thermograms confirmed additionally the presence of both compounds (see Figure S6).

Confocal Raman spectroscopy was used to identify the arrangement of ADN and HMX in the obtained particles.

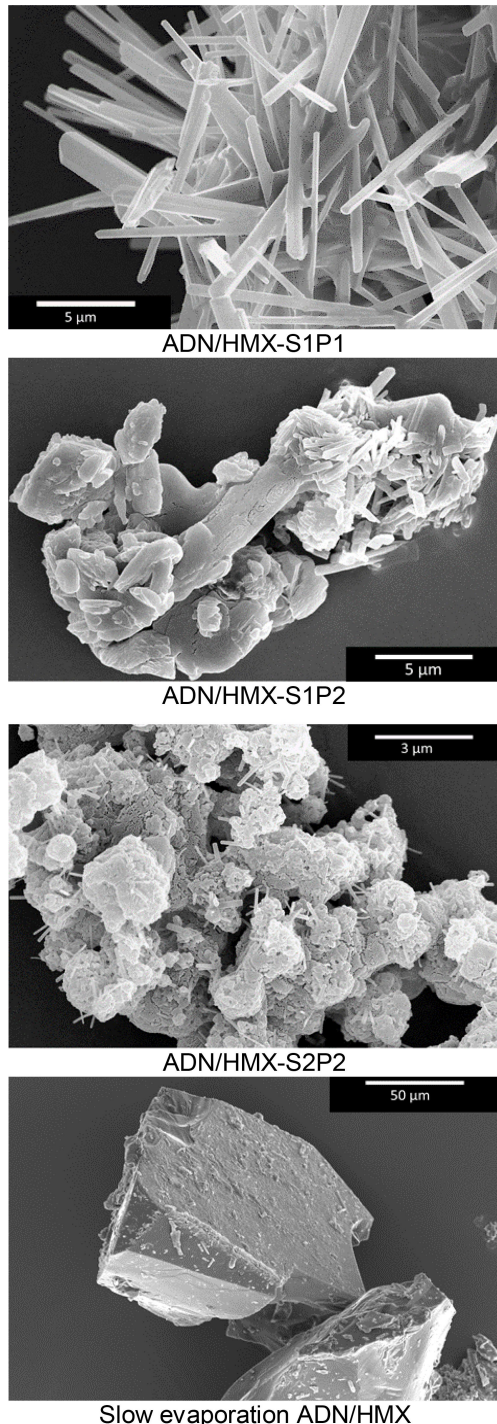


Figure 6. SEM pictures of the ADN/HMX.

HMX is identified by the symmetric -CH stretching vibration appearing at  $2995\text{ cm}^{-1}$ .

ADN is highlighted within confocal Raman maps by the O—N—O bending vibration localized at  $829\text{ cm}^{-1}$ . Raman spectra are shown in Figure 9C for pure compounds and no overlap was noticed (Figure 9C). However, slow crystal-

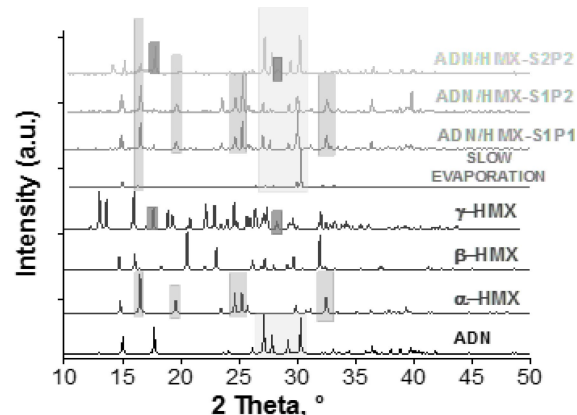


Figure 7. Diffraction patterns for the ADN/HMX composites.

Table 6. Crystallographic forms and crystallite sizes ( $2\theta = 25.04^\circ$ ).

Composite	Operating conditions	Crystallite size, nm	Polymorphism for the explosive
ADN/HMX	Slow evaporation	49.9	$\alpha$
	HMX-S1P1	72.5	$\alpha$
	HMX-S1P2	76.5	$\alpha$
	HMX-S2P2	75.9	$\gamma + \alpha$

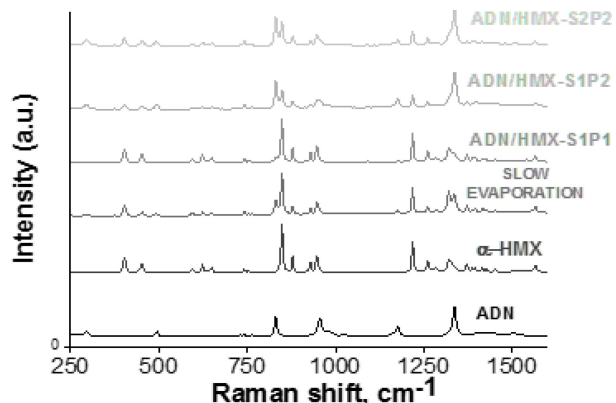
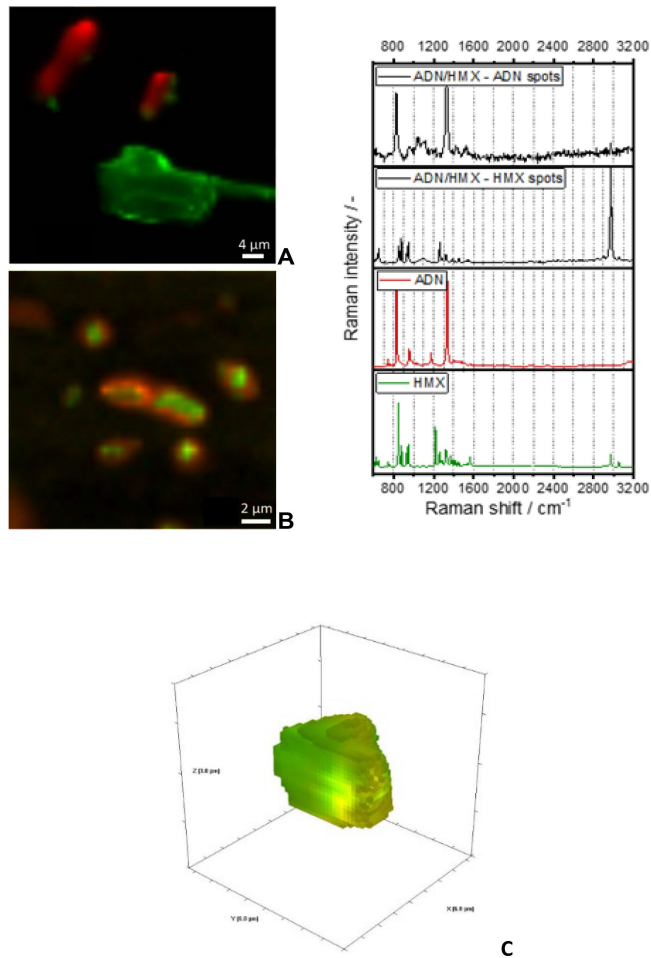


Figure 8. Raman spectra for ADN, HMX and the ADN/HMX composites.

lization leads to the formation of separate HMX and ADN particles. ADN/HMX-S2P2 Raman maps show HMX particles within an ADN droplet as already described for SFE-produced ADN/RDX particles. Consequently, a similar core-shell particle formation is supposed (Figure 9C).

	RAMAN SHIFT, cm <sup>-1</sup>	ASSIGNEMENT
ADN [32]	297	δ stretching N-N-N
	491	δ wag NO <sub>2</sub> in phase
	829	δ sciss NO <sub>2</sub> in phase
	955	v s N <sub>3</sub>
	1177	v s NO <sub>2</sub> out of phase
α-HMX [46, 47]	402	Movement vib vs (NC <sub>2</sub> )
	848	b(ONO), vs (NNC <sub>2</sub> )
	877	vs (NNC <sub>2</sub> )
	929	v (NN), b(ONO)
	946	
	956	
	1218	vas (NC <sub>2</sub> )



**Figure 9.** ADN/HMX composites obtained by A) slow evaporation and B) SFE 4 MPa, 110 °C in methyl acetate (ADN/HMX-S2P2).

## 3.4 Sensitivities and Reactivity

### 3.4.1 Sensitivities

Impact, friction and electrostatic discharge sensitivity tests were carried out on pristine materials, pristine materials recrystallized by SFE and all ADN containing composites. These tests are provided to qualitatively compare the sensitivity of the different formulated materials with pure sec-

ondary explosive or ADN recrystallized in the same operating conditions. The results are summed up in Table 7.

In the case of RDX, the ESD threshold increases by decreasing the size and adding ADN in the formulation. The product becomes insensitive to friction. The compounds obtain by SFE present higher impact sensitivity. This point will be discussed part 3.7.

In the case of HMX, the ESD threshold is higher by decreasing size or adding ADN compared to the initial raw materials. The composites are not sensitive to friction and the same decreasing of the impact threshold is obtained.

The composites obtained by slow evaporation present higher sensitivity thresholds in the case of RDX. In the case of HMX, slow evaporation provides lower sensitivity thresholds than the one of the composites obtained by SFE. This compound is clearly unsuitable for further handling. In this case, the effect of the downsizing could be an explanation but the opposite trend is obtained for RDX. Slow evaporation leads to a micron size and coarse mixture between both components as suggested by the morphology studies in section 3.2 and 3.3.

### 3.4.2 Reactivity

As already described in part 2.3.2, the PMMA tubes are filled with the diverse powders. The percentage of the theoretical maximal density (TMD) is evaluated by measuring the mass of the powder (*m*) in the tube and its height (*h*) and evaluate according to equation 3, with  $\rho$  density of explosive crystal (Table 1):

$$\% \text{ TMD} = \frac{m}{\pi \cdot 0.15^2 \cdot h \cdot \rho} \quad (3)$$

Single frames recorded by the high-speed camera allow to measure the distance covered by the flame during a time interval defined by the video speed (frame by second). The length of the tube is used as reference. The distance to time curve is presented for instance in Figure 10 (I-B and II-B). The transition distance from deflagration to detonation (DDTD) is characterized by a distance and a time corresponding to the change of slope. There is a linear relationship between distance and time in case of detonation. The slope directly provides the detonation velocities  $V_D$ . The distance is not subject to a regular evolution with time in case of deflagration. The secondary derivative with time provides the acceleration.

Table 8 summarizes the main energetic performance evaluated for pure compounds obtained by SFE and composites. Under the investigated conditions, all pure secondary explosives can ignite except HMX (see also Figure S7) despite different loadings (4.5 to 30%TMD). ADN/HMX composites detonate with a  $V_D$  of 3.2 km.s<sup>-1</sup> and 3.6 km.s<sup>-1</sup> with loading density of 17.5% and 24.4% TMD. For all composites, significative higher loading densities are obtained

**Table 7.** Impact, friction and electrostatic discharge sensitivity of different pyrotechnic compositions (raw material, sole material obtained by SFE, composite obtained either by SFE or slow evaporation).

	Composition	Impact (J)	Friction (N)	ESD (mJ)	Polymorphism	Particle shape
Raw materials	RDX EURENCO	4,0	160	120	$\alpha$	—
	HMX EURENCO	5,0	120	230	$\beta$	—
	ADN	3	> 360	1496	—	—
Pure component <sup>[a]</sup>	RDX	< 1,6	> 360	261	$\alpha$	Spherical
	HMX	3,0	> 360	1212	$\gamma + \alpha$	Spherical
Composite <sup>[b]</sup>	Nano ADN	4,5	> 360	996	—	Spherical
	ADN/RDX	1,6	> 360	477	$\alpha$	Ovoidal
	ADN/HMX	2,1	> 360	957	$\alpha$	Rod
Slow evaporation	ADN/RDX	4,5	> 360	957	$\alpha$	—
	ADN/HMX	1,6	128	268	$\alpha$	—

<sup>[a]</sup> SFE, 110 °C, 2 MPa <sup>[b]</sup> SFE, acetone, 110 °C, 2 MPa.**Table 8.** Reactivity tests performed with powder obtained by SFE process (acetone, 110 °C, 2 MPa) either on the pure product or on the composite (LP: loose powder).

Powder	Stack in tube	TMD%	$V_D$ $m s^{-1}$	DDTD <sub>m</sub>	$\Delta V_D$ $m s^{-1}$	$\Delta DDTD$ m
HMX	packed	9.50	NO DETONATION			
	LP	5.60				
RDX	packed	16.00	3358	0.021	125	0.013
	LP	8.20	2743			
ADN	packed			0.012	87	0.004
	LP	16.31	1920			
ADN/HMX	packed	24.40	3636	0.006	133	0.001
	LP	17.50	3181			
ADN/RDX	packed	37.20	3359	0.010	72	0.025
	LP	26.5	2806			

compared to pure explosive. The oxidizer contributes to promote the loading by improving the flowability of the powder. Similar or higher detonation velocities are obtained for the composite due to higher TMDs and OBs close to 0%. Better results in term of reactivity were obtained with composites: indeed, DDTD of RDX and ADN/RDX are measured respectively at 20.8 mm and 9.5 mm. This DDTD is even shorter in case of ADN/HMX with a value of 6 mm.

### 3.5 Discussion on the Effect of the Process Parameters on the Morphology of the Particles

The effect of the nozzle pressure is studied by using acetone as solvent for pristine secondary explosives and composites. Pressure acts on the flowrate. It will affect indirectly the evaporation, because the exhaust gas capacity remains unchanged whereas a higher gas amount is released. It modifies then the evolution of supersaturation inside the droplet and consequently, modifies the particle properties by changing nucleation conditions. For pure explosive compounds, increasing the pressure increases the mean particle size (Table 4 and Figure 1). The amount of solution is higher for the same vacuum pumping and solvent build up in the

chamber. The residence time is shortened and the accumulation could contribute to the redissolution of particles on the filter.

As shown in the Figures 2, 6 and 10, composite particles are larger than those of pure explosives or pure ADN. At lower pressure, it seems that the particles tend to agglomerate by using acetone as solvent. Acetone is the solvent for which all the compounds present the highest solubility. The supersaturation is then lately reached. Nucleation occurs in a small volume of solvent and contact between nuclei will be favored, promoting particle growth. The solubility is particularly high for ADN. This mechanism is favored by the longer residence time, set by the pressure.

The solvent choice is a crucial parameter because it concomitantly affects thermodynamics (evaporation), solubility of the solute and kinetics of crystallization. Regarding the solubility in acetone (S1), ADN is more soluble than RDX and HMX. During the evaporation process, the explosive (RDX or HMX) crystallizes first and then ADN reaches its supersaturation and starts crystallization in turn. Solubility of each explosive and ADN were reported in Table 2. On top of the solubility difference, ADN has a lower melting point, set to 95 °C, at ambient pressure (Table 2). For the ADN/HMX-S2P2, methyl acetate solvent was used. The solubility in methyl acetate is lower than in acetone as well as the evaporation rate. It leads to a faster evaporation and then to a faster nucleation. It explains the size reduction of the particles.

### 3.6 ADN/Secondary Explosive Composites: Discussion on the Core-Shell Structure and Polymorphism

Secondary explosives were initially used in their most stable form, *i.e.*  $\alpha$ -RDX,  $\beta$ -HMX and  $\epsilon$ -CL-20. After recrystallization, for pure secondary explosive, RDX remains in the  $\alpha$  form and orthorhombic  $\alpha$ -HMX is obtained by recrystallization of pristine HMX, either directly or first in  $\gamma$  which progressively evolves in  $\alpha$  with age of the formulated materials or in  $\beta$  in case of methyl acetate as solvent. The crystallization occur-

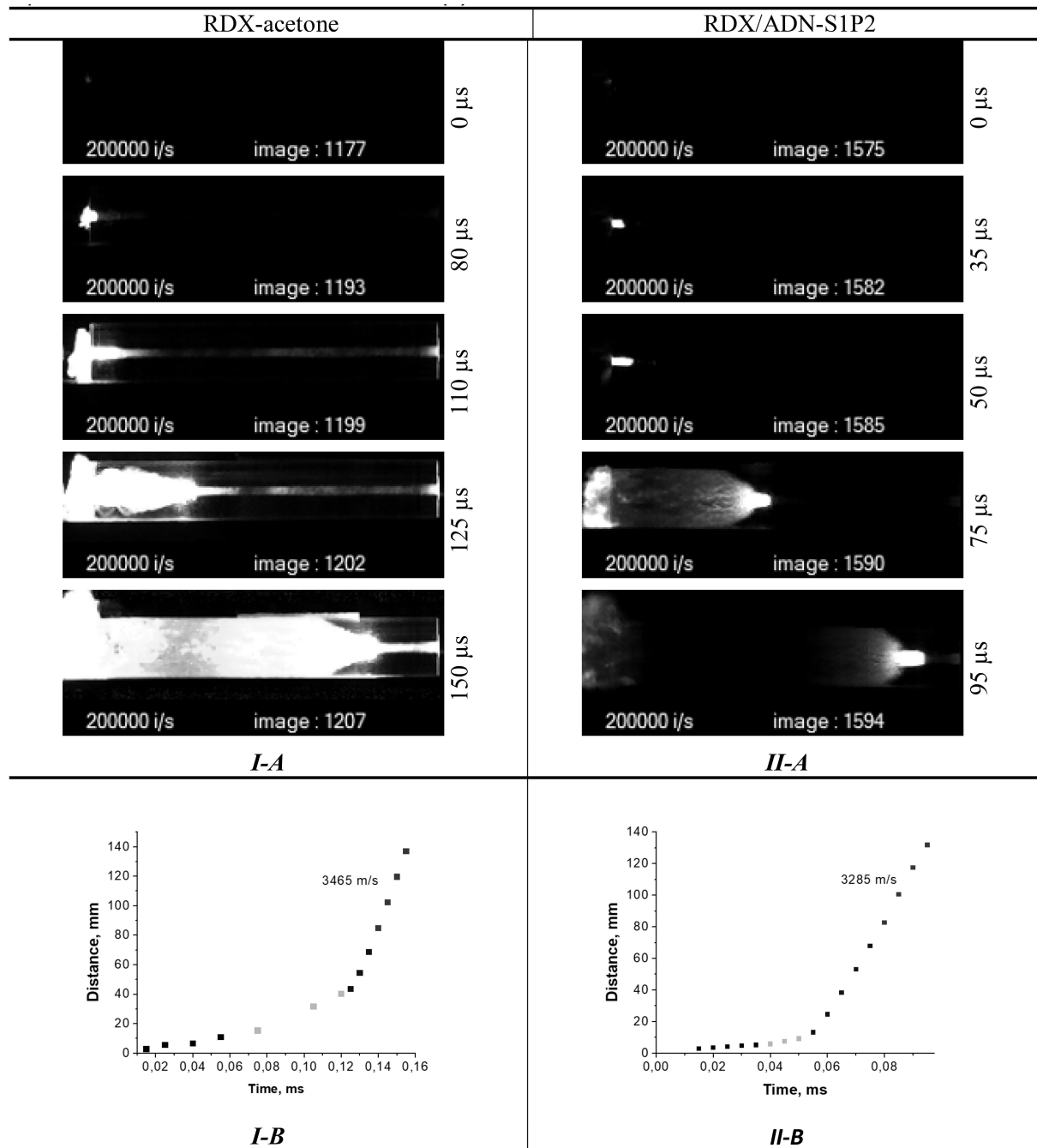


Figure 10. Reactivity tests and velocity measurements for RDX S1P2 (I) and ADN/RDX composite S1P2 (II). (A) represents the record of detonation test in tube (B) the distance/time curve.

ring in the SFE process, like in the spray method used by Singh *et al.* [48], is kinetically driven and consequently produces mostly metastable phase. The polymorphism is affected by the supersaturation. The most stable form will be obtained if the system is able to reach its thermodynamic state. The metastable form of the crystal could be obtained according to the residence time of the crystal in its solvent. In particular, at the initial stage of the crystallization, a

metastable form will be obtained during the transition of the saturated solution to the supersaturated solution. The next steps will be affected by the nucleation kinetics, lattice growth rate and obviously by the evaporation rate which drives the time during which the crystal is in the solvent. In literature, it is mentioned that HMX could stay in  $\alpha$  form at room temperature without adding solvent [49]. The transition between the two polymorphs occurs at temperatures

ranging from 102°C to 150°C. However, during the dissolution in acetone the crystal morphology may be altered because the solvent molecules act as nucleation site. In acetone, it was demonstrated that this solvation effect promotes phase transition and reduces transition temperature. Consequently, at low temperature in solvent (i.e. below 500 K), the dissolved  $\beta$  form crystallizes in the  $\alpha$  form in presence of solvent, the  $\alpha$  form is thermodynamically stable in a temperature regime that falls between  $\beta$  and  $\delta$  regions [49]. Fast crystallization process and the solvent used promotes here the  $\alpha$  form due to the solvent choice and the  $\beta$  form required a longer time of the crystal in solution [50]. In the composite, the  $\alpha$  form is always obtained.

The morphology of the composites crystallized by SFE enables to obtain core-shell particles. Due to the formation of ADN droplets below secondary explosive particles, confocal Raman spectroscopy data point to the formation of secondary explosive cores and ADN shells. The formation of these ADN droplets is explained by self-dissolution of the ADN shell in ambient water because of its high hygroscopicity. The explanation is based on two facts. First, the melting point of the ADN is low at ambient pressure. Sublimation of the ADN molecules may occur without additives in the operating conditions used in SFE. Pristine ADN was not recovered on filters by using acetone as solvent contrary to ethyl or methyl acetate. Molecules with these thermal properties need often to an anchoring to avoid sublimation as previously mentioned for trinitrotoluene (TNT, MP:80°C [15]). Second, the formation of these core-shell particles could be explained by the solubility of the compounds in solvent. Indeed, the secondary explosive is less soluble than the ADN. Inside the droplets generated by spray, the concentration of the solutes progressively increases during evaporation. The secondary explosive reaches its supersaturation faster and starts consequently its nucleation process. These nuclei agglomerate while evaporation proceeds. During the further evaporation, ADN supersaturation is reached in turn and the nucleation occurs on top of primary formed secondary explosive particles. A quite similar mechanism was described and deeply investigated by Hübner *et al.* [45].

### 3.7 ADN/Secondary Explosive Composite: Sensitivity and Reactivity

Regarding sensitivity, an astonishing result catches our attention. For secondary explosives, SFE crystallization induces systematically higher impact sensitivity compared to raw material. In the SFE process used in this paper, particles are collected on a filter enclosed in a glass container. Depending on the method for particles collection, sensitivities of energetic materials regarding impact and ESD are drastically modified as presented in Table 9.

In the system used in this publication, particles buildup electrical charge at their surfaces due to the motion inside the glass vessel. As a consequence, they exhibit a highest sensitivity to impact. Indeed, impact test measures the response to the solicitation for the global sample weight. Moreover, Bidault and Pineau performed simulations on RDX grains by studying the effect of the nanograin size and porosity on the shock sensitivity [53]. They demonstrate that porosity affects the sensitivity. Here, the particle agglomeration on the filter could also be responsible for this shock sensitivity increase.

Nevertheless, the comparison between pure components and mixtures make sense because they were obtained under same operating conditions and recovered with the same system. Parameters which can affect the sensitivity are particles size, shape and the polymorphism. RDX is in  $\alpha$  form in both pristine and composite particles. HMX was obtained in the  $\alpha$  form too in the investigated conditions contrary to the neat product. This change of crystallographic polymorphism may lead to more sensitive compounds in addition of the size reduction effect.

According to literature, OBs close to zero were supposed to decrease the impact sensitivity which is not the case in the composites obtained [24]. The size obtained for the ADN/secondary explosive composites is also larger than those of pure components with micrometric scale suggesting the possibility of local defects responsible for higher sensitivity. The polymorphism of secondary explosives can also explain this trend.

Sensitivities results demonstrate that the ADN/secondary explosive composites remain relatively few sensitive to ESD and friction. ADN features, as identified in previous work, impact on explosive mixtures safety. This could be due to the core-shell structure of the ADN/secondary ex-

**Table 9.** Sensitivity of secondary explosive depending on the way of particle collection for RDX in acetone.

Impact, J	Friction, N	ESD, mJ	Particle collection	Operating conditions, (P,T)	Concentration, wt %	Mean size, nm	Morphology and phase	Ref
3	180	200	Filter	4 MPa, 160 °C	2	300	Spherical, $\alpha$	[19]
4	288	249	Filter		2	80		[51]
2.05	180	359	Cyclone		3	~500		[52]
<1.6	>360	261	Filter + glass container	2 MPa 110 °C	1	320 +/- 2.8		

plosives: Since ADN is less sensitive to ESD, ADN shells may protect secondary explosive cores.

Regarding detonation velocity tests, all ADN/secondary explosive pyrotechnic compositions lead to detonation in the investigated conditions (Table 9). Thus, ADN is supposed to promote the detonation of secondary explosives.

To resume, we succeed in formulating energetic composite materials that improve reactivity of secondary explosives, by decreasing the DDTD or, just by allowing the decomposition in a given loading diameter. In each case, oxidizer facilitates tube loading for a given operating method by increasing the %TMD. Additional studies should be conducted to determine maximum velocity of detonation reached by theses composite materials by varying ratio and %TMD.

## 4 Conclusion

This study underlines that the spray flash evaporation process is an effective way to combine ADN and explosives to form a composite with fixed OB. This work highlights versatile aspects of SFE which allows to crystallize explosives with oxidizer. Submicronic composites with intimate mixtures of both compounds were successfully obtained. Moreover, this process is efficient and reliable given that the proportion of both compounds is maintained in the final powder. It allows to obtain quickly a ready-to-use pyrotechnic composition by limiting the formulation preparation. The main limiting factor is the solubility of the compounds in suitable solvents for SFE process.

The use of different advanced analytical techniques highlights the core/shell structure of the obtained particles and provide some useful information to bring some insights on the crystallization mechanisms occurring in the SFE process regarding size control, polymorphism and particle morphology.

One of the purposes of this work was to study the benefit of mixing secondary explosive and oxidizer. The results obtained are encouraging and show moderate improvements in friction and ESD sensitivity threshold. Outstanding reactivity performances are yet obtained. These energetic compositions detonate in small tube even for the HMX based composite contrary to pristine HMX. The interesting point is the short DDTD obtained and even reduced for both compounds. This first study paves the way to further investigations to improve formulation.

## Symbols and Abbreviations

ADN	Ammonium DiNitramide
CL-20	2,4,6,8,10,12,-hexanitro-2,4,6,8,10,12-hexaaazaisowurtzitane or HNIW
DDTD	Deflagration-to-Detonation Transition Distance
DFT	Density Functional Theory

DT	Decomposition Temperature
ESD	ElectroStatic Discharge
HMX	1,3,5,7-tetranitro-1,3,5,7-tetraazacyclooctane or octogen
MP	Melting Point
ONC	OctaNitroCubane
RDX	1,3,5-trinitro-1,3,5-triazacyclohexane or hexogen
SFE	Spray Flash Evaporation
TMD	Theoretical Maximal Density
TNT	2-methyl-1,3,5-trinitrobenzene or 2,4,6-trinitrotoluene
TTTO	tetrazino-tetrazine-tetraoxide
V <sub>D</sub>	Detonation velocity

## Acknowledgements

The authors would like to thank the ISL photographers M. Yanick Boehrer and Yves Suma, the ISL workshop for the SFE pilot and the PMMA tubes. Moreover, the authors thanks to Dr. Marc Comet for its help on the detonation tests and M. Philippe Fioux from IS2 M for XPS analyses. The PhD was funded by the ISL. Financially supported ISL.

## Data Availability Statement

Data available on request due to privacy/ethical restrictions.

## References

- [1] N. Zohari, M. H. Keshavarz, S. A. Seyedsadjadi, The Advantages and Shortcomings of Using Nano-Sized Energetic Materials. *Cent. Eur. J. Energ. Mater.* **2013**, *10*, 135–147.
- [2] V. Stepanov, V. Anglade, W. A. Balas Hummers, A. V. Bezmelnitsyn, L. N. Krasnoperov, Production and Sensitivity Evaluation of Nanocrystalline RDX-Based Explosive Compositions. *Propellants, Explosives, Pyrotechnics* **2011**, *36*, 240–246. <https://doi.org/10.1002/prep.201000114>.
- [3] N. Radacsi, R. H. B. Bouma, E. L. M. Krabbendam-la Haye, J. H. ter Horst, A. I. Stankiewicz, A. E. D. M. van der Heijden, On the Reliability of Sensitivity Test Methods for Submicrometer-Sized RDX and HMX Particles. *Propellants, Explosives, Pyrotechnics* **2013**, *38*, 761–769. <https://doi.org/10.1002/prep.201200189>.
- [4] Y. Bayat, V. Zeynali, Preparation and Characterization of Nano-CL-20 Explosive. *Journal of Energetic Materials* **2011**, *29*, 281–291. <https://doi.org/10.1080/07370652.2010.527897>.
- [5] J. Liu, W. Jiang, Q. Yang, J. Song, G. Hao, F. Li, Study of Nano-Nitramine Explosives: Preparation, Sensitivity and Application. *Defence Technology* **2014**, *10*, 184–189. <https://doi.org/10.1016/j.dt.2014.04.002>.
- [6] F. Pessina, D. Spitzer, The Longstanding Challenge of the Nanocrystallization of 1,3,5-Trinitroperhydro-1,3,5-Triazine (RDX). *Beilstein Journal of Nanotechnology* **2017**, *8*, 452–466. <https://doi.org/10.3762/bjnano.8.49>.
- [7] P. Redner, D. Kapoor, R. Patel, M. Chung, D. Martin, *Production and Characterization of Nano-RDX*; DTIC Document ADA481870, 2006.
- [8] Y. Wang, W. Jiang, X. Song, G. Deng, F. Li, Insensitive HMX (Octahydro-1,3,5,7-Tetranitro-1,3,5,7-Tetrazocine) Nanocrystals

- Fabricated by High-Yield, Low Cost Mechanical Milling. *Cent. Eur. J. Energ. Mater.* **2013**, *10*, 277–287.
- [9] N. Radacsi, R. Ambrus, T. Szunyogh, P. Szabó-Révész, A. Stankiewicz, A. van der Heijden, J. H. ter Horst, Electrospray Crystallization for Nanosized Pharmaceuticals with Improved Properties. *Crystal Growth & Design* **2012**, *12*, 3514–3520. <https://doi.org/10.1021/cg300285w>.
- [10] B.-M. Lee, D. S. Kim, Y.-H. Lee, B.-C. Lee, H.-S. Kim, H. Kim, Y.-W. Lee, Preparation of Submicron-Sized RDX Particles by Rapid Expansion of Solution Using Compressed Liquid Dimethyl Ether. *The Journal of Supercritical Fluids* **2011**, *57*, 251–258. <https://doi.org/10.1016/j.supflu.2011.03.008>.
- [11] J. T. Essel, A. C. Cortopassi, K. K. Kuo, J. H. Adair, C. G. Leh, T. M. Klapoetke, *Synthesis of Energetic Materials by Rapid Expansion of a Supercritical Solution into Aqueous Solution (RESS-AS) Process*; DTIC Document ADA544674, **2010**.
- [12] H. Qiu, V. Stepanov, A. R. Di Stasio, T. Chou, W. Y. Lee, RDX-Based Nanocomposite Microparticles for Significantly Reduced Shock Sensitivity. *Journal of Hazardous Materials* **2011**, *185*, 489–493. <https://doi.org/10.1016/j.jhazmat.2010.09.058>.
- [13] J.-W. Kim, M.-S. Shin, J.-K. Kim, H.-S. Kim, K.-K. Koo, Evaporation Crystallization of RDX by Ultrasonic Spray. *Industrial & Engineering Chemistry Research* **2011**, *50*, 12186–12193. <https://doi.org/10.1021/ie201314r>.
- [14] J. W. Kim, H. M. Shim, J. K. Kim, M. S. Shin, H. S. Kima, K. K. Koo, Effect Of Polyvinylpyrrolidone On Crystallization Of Rdx By Ultrasonic Spray. In *18th International Symposium on Industrial Crystallization*; September 13–16, **2011**.
- [15] A. Sèvre, V. Pichot, F. Schnell, D. Spitzer, Trinitrotoluene Nanostructuring by Spray Flash Evaporation Process. *Propellants, Explosives, Pyrotechnics* **2017**, *42*, 1051–1056. <https://doi.org/10.1002/prep.201700024>.
- [16] V. Pichot, A. Seve, J. Berthe, F. Schnell, D. Spitzer, Study of the Elaboration of HMX and HMX Composites by the Spray Flash Evaporation Process. *Propellants, Explosives, Pyrotechnics* **2017**, *42*, 1418–1423. <https://doi.org/10.1002/prep.201700171>.
- [17] A. N. Zhigach, I. O. Leipunskii, A. N. Pivkina, N. V. Muravyev, K. A. Monogarov, M. L. Kuskov, E. S. Afanasenkova, N. G. Berezhkina, P. A. Pshechenkov, A. A. Bragin, Aluminium/HMX Nanocomposites: Synthesis, Microstructure and Combustion. *Combustion, Explosion and Shock Waves* **2015**, *51*, 100–106. <https://doi.org/10.1134/S0010508215010104>.
- [18] T. Liu, C. Geng, B. Zheng, S. Li, G. Luo, Encapsulation of Cyclotetramethylenetrinitramine (HMX) by Electrostatically Self-Assembled Graphene Oxide for Desensitization. *Propellants, Explosives, Pyrotechnics* **2017**, *42* (9), 1057–1065. <https://doi.org/10.1002/prep.201700053>.
- [19] M. Guillevic, V. Pichot, P. Fioux, F. Schnell, D. Spitzer, Nano-diamond-Based Energetic Core-Shell Composites: The Route towards Safer Materials. *Diamond and Related Materials* **2019**, *93*, 150–158. <https://doi.org/10.1016/j.diamond.2019.02.006>.
- [20] J. T. Essel, A. C. Cortopassi, K. K. Kuo, C. G. Leh, J. H. Adair, Formation and Characterization of Nano-Sized RDX Particles Produced Using the RESS-AS Process. *Propellants, Explosives, Pyrotechnics* **2012**, *37*, 699–706. <https://doi.org/10.1002/prep.201100139>.
- [21] W. C. Lothrop, G. R. Handrick, The Relationship between Performance and Constitution of Pure Organic Explosive Compounds. *Chem. Rev.* **1949**, *44*, 419–445. <https://doi.org/10.1021/cr60139a001>.
- [22] J. Akhavan, *The Chemistry of Explosives*, The Royal Society of Chemistry, **2011**.
- [23] E. S. Shanley, G. A. Melhem, The Oxygen Balance Criterion for Thermal Hazards Assessment. *Process Safety Progress* **1995**, *14*, 29–31. <https://doi.org/10.1002/prs.680140105>.
- [24] M. J. Kamlet, H. G. Adolph, The Relationship of Impact Sensitivity with Structure of Organic High Explosives. II. Polynitroaromatic Explosives. *Propellants, Explosives, Pyrotechnics* **1979**, *4*, 30–34. <https://doi.org/10.1002/prep.19790040204>.
- [25] M.-X. Zhang, P. E. Eaton, R. Gilardi, Hepta- and Octanitrocubanes. *Angewandte Chemie International Edition* **2000**, *39*, 401–404. [https://doi.org/10.1002/\(SICI\)1521-3773\(20000117\)39:2<401::AID-ANIE401>3.0.CO;2-P](https://doi.org/10.1002/(SICI)1521-3773(20000117)39:2<401::AID-ANIE401>3.0.CO;2-P).
- [26] M. S. Klenov, A. A. Guskov, O. V. Anikin, A. M. Churakov, Y. A. Strelenko, I. V. Fedyanin, K. A. Lyssenko, V. A. Tartakovsky, Synthesis of Tetrazino-tetrazine 1,3,6,8-Tetraoxide (TTTO). *Angew. Chem. Int. Ed.* **2016**, *4*.
- [27] Q. Wu, W. Zhu, H. Xiao, A New Design Strategy for High-Energy Low-Sensitivity Explosives: Combining Oxygen Balance Equal to Zero, a Combination of Nitro and Amino Groups, and N-Oxide in One Molecule of 1-Amino-5-Nitrotetrazole-3 N-Oxide. *J. Mater. Chem. A* **2014**, *2*, 13006–13015. <https://doi.org/10.1039/C4TA01879F>.
- [28] P. He, J.-G. Zhang, K. Wang, X. Yin, T.-L. Zhang, Combination Multinitrogen with Good Oxygen Balance: Molecule and Synthesis Design of Polynitro-Substituted Tetrazolotriazine-Based Energetic Compounds. *J. Org. Chem.* **2015**, *80*, 5643–5651. <https://doi.org/10.1021/acs.joc.5b00545>.
- [29] R. Meyer, J. Köhler, A. Homberg, *Explosives*, 6th edition.; Wiley-VCH Verlag GmbH & Co. KGaA, Weinheim **2008**.
- [30] Koch, Ernst-Christian, *Sprengstoffe, Treibmittel, Pyrotechnika*, Lutradyn Kaiserslautern; **2017**.
- [31] M. Nagamachi, J. I. Oliveira, A. M. Kawamoto, R. de C. L. Dutra, ADN - The New Oxidizer around the Corner for an Environmentally Friendly Smokeless Propellant. *Journal of Aerospace Technology and Management* **2009**, *1*, 153–160.
- [32] H. Östmark, U. Bemm, A. Langlet, R. Sandén, N. Wingborg, The Properties of Ammonium Dinitramide (ADN): Part 1, Basic Properties and Spectroscopic Data. *Journal of Energetic Materials* **2000**, *18*, 123–138. <https://doi.org/10.1080/07370650008216116>.
- [33] N. Wingborg, Ammonium Dinitramide-Water: Interaction and Properties. *J. Chem. Eng. Data* **2006**, *51*, 1582–1586.
- [34] L. Blas, M. Klaumünzer, F. Pessina, S. Braun, D. Spitzer, Nanostructuring of Pure and Composite-Based K6 Formulations with Low Sensitivities. *Propellants, Explosives, Pyrotechnics* **2015**, *40*, 938–944. <https://doi.org/10.1002/prep.201500187>.
- [35] J.-E. Berthe, F. Schnell, Y. Boehler, D. Spitzer, Nano-crystallisation of Ammonium DiNitramide (ADN) by Spray Flash Evaporation (SFE). *Propellants, Explosives, Pyrotechnics* **2018**, *43*, 609–615. <https://doi.org/10.1002/prep.201800039>.
- [36] A. Le Brize, D. Spitzer, Plasticization of Submicron-Structured LOVA Propellants by a Linear Dinitramine. *Central European Journal of Energetic Materials* **2016**, *13*, 547–556.
- [37] D. Spitzer, B. Risse, F. Schnell, V. Pichot, M. Klaumünzer, M. R. Schaefer, Continuous Engineering of Nano-Cocrystals for Medical and Energetic Applications. *Sci. Rep.*, **2014**, *4*. <https://doi.org/10.1038/srep06575>.
- [38] B. Risse, D. Spitzer, D. Hassler, F. Schnell, M. Comet, V. Pichot, H. Muhr, Continuous Formation of Submicron Energetic Particles by the Flash-Evaporation Technique. *Chemical Engineering Journal* **2012**, *203*, 158–165. <https://doi.org/10.1016/j.cej.2012.07.032>.
- [39] H. Östmark, A. Helte, S. Karlsson, A. Hahma, H. Edvinsson, Detonation Properties and Reaction Rate Modeling of Melt Cast Ammonium Dinitramide (ADN). In *Proceedings of the 12th Inter-*

- national Detonation Symposium; August 11–16, 2002;* pp 11–16.
- [40] M. E. Sitzmann, S. Foti, C. C. Misener, *Solubilities of High Explosives: Removal of High Explosive Fillers from Munitions by Chemical Dissolution*; DTIC Document AD773078, 1973.
- [41] G. Santhosh, Investigations on the Physical, Chemical and Electrochemical Properties of Ammonium Dinitramide (ADN), 2005.
- [42] S. Löbbecke, H. H. Krause, A. Pfeil, Thermal Analysis of Ammonium Dinitramide Decomposition. *Propellants, Explosives, Pyrotechnics* 1997, 22, 184–188. <https://doi.org/10.1002/prep.19970220317>.
- [43] D. E. G. Jones, Q. S. M. Kwok, M. Vachon, C. Badeen, W. Ridley, Characterization of ADN and ADN-Based Propellants. *Propellants, Explosives, Pyrotechnics* 2005, 30, 140–147. <https://doi.org/10.1002/prep.200400096>.
- [44] J. Hübner, T. Deckert-Gaudig, J. Glorian, V. Deckert, D. Spitzer, Surface Characterization of Nanoscale Co-Crystals Enabled through Tip Enhanced Raman Spectroscopy. *Nanoscale* 2020, 12, 10306–10319. <https://doi.org/10.1039/D0NR00397B>.
- [45] J. Hübner, V. Pichot, E. Lobry, T. Deckert-Gaudig, V. Deckert, D. Spitzer, Formation Mechanism of Anisotropic RDX-TNT Core-Shell Nanoparticles and Their Influence onto Nanodiamond Detonation Syntheses. 2020. <https://doi.org/10.26434/chemrxiv.12005625.v1>.
- [46] F. Goetz, T. B. Brill, Laser Raman Spectra of .alpha.-, .beta.-, .gamma.-, and .delta.-Octahydro-1,3,5,7-Tetranitro-1,3,5,7-Tetrazocine and Their Temperature Dependence. *J. Phys. Chem.* 1979, 83, 340–346. <https://doi.org/10.1021/j100466a008>.
- [47] H. V. Brand, R. L. Rabie, D. J. Funk, I. Diaz-Acosta, P. Pulay, T. K. Lippert, Theoretical and Experimental Study of the Vibrational Spectra of the A, B, and Δ Phases of Octahydro-1,3,5,7-Tetranitro-1,3,5,7-Tetrazocine (HMX). *J. Phys. Chem. B* 2002, 106, 10594–10604. <https://doi.org/10.1021/jp020909z>.
- [48] H. Singh, N. Jahagirdar, S. Banerjee, Sonochemically Assisted Synthesis of Nano HMX. *Defence Technology* 2019, 15, 837–843. <https://doi.org/https://doi.org/10.1016/j.dt.2019.04.010>.
- [49] P. C. Myint, A. L. Nichols, Thermodynamics of HMX Polymorphs and HMX/RDX Mixtures. *Ind. Eng. Chem. Res.* 2017, 56, 387–403. <https://doi.org/10.1021/acs.iecr.6b03697>.
- [50] M. Ghosh, S. Banerjee, M. A. Shafeeuulla Khan, N. Sikder, A. K. Sikder, Understanding Metastable Phase Transformation during Crystallization of RDX, HMX and CL-20: Experimental and DFT Studies. *Phys. Chem. Chem. Phys.* 2016, 18, 23554–23571. <https://doi.org/10.1039/C6CP02185A>.
- [51] M. Guillevic, V. Pichot, F. Ciszek, D. Spitzer, Heat Dissipating Nanodiamonds for Desensitization of Composite Materials. In *50th International Annual Conference of ICT*; Karlsruhe, Germany, June 25–28, 2019.
- [52] F. Pessina, F. Schnell, D. Spitzer, Tunable Continuous Production of RDX from Microns to Nanoscale Using Polymeric Additives. *Chemical Engineering Journal* 2016, 291, 12–19. <https://doi.org/10.1016/j.cej.2016.01.083>.
- [53] X. Bidault, N. Pineau, Granularity Impact on Hotspot Formation and Local Chemistry in Shocked Nanostructured RDX. *J. Chem. Phys.* 2018, 149, 224703. <https://doi.org/10.1063/1.5049474>.

Manuscript received: April 15, 2020

Revised manuscript received: October 12, 2020

Version of record online: January 18, 2021